Rock Mechanics and Rock Engineering manuscript No.
(will be inserted by the editor)

Micro-macro analysis and phenomenological modelling of salt viscous damage and application to salt caverns

Cheng Zhu · Ahmad Pouya · Chloé Arson

Received: date / Accepted: date

Abstract This paper aims to gain fundamental understanding of the microscopic mechanisms that control the transition between secondary and tertiary creep around salt caverns in typical geological storage conditions. We use a self-consistent inclusion-matrix model to homogenize the visco-plastic deformation of halite polycrystals and predict the number of broken grains in a Representative Elementary Volume of salt. We use this micro-macro modeling framework to simulate creep tests under various axial stresses, which gives us the critical visco-plastic strain at which grain breakage (i.e. tertiary creep) is expected to occur. The comparison of simulation results for short-term and long-term creep indicates that the initiation of tertiary creep depends on the stress and the viscoplastic strain. We use the critical viscoplastic deformation as a yield criterion to control the transition between secondary and tertiary creep in a phenomenological viscoplastic model, which we implement into the Finite Element Method program POROFIS. We model a 850m-deep salt cavern of irregular shape, in axis-symmetric conditions. Simulations of cavern depressurization indicate that a strain-dependent damage evolution law is more suitable than a stress-dependent damage evolution law, because it avoids high damage concentrations and allows capturing the formation of a damaged zone around the cavity. The modeling framework explained in this paper is expected to provide new insights to link grain breakage to phenomenological damage variables used in Continuum Damage Mechanics.

Keywords salt rock · creep · viscoplastic deformation · damage · micro-macro model · Finite Element Method · geological storage

C. Zhu
School of Civil and Environmental Engineering,
Georgia Institute of Technology,
790 Atlantic Drive, Atlanta, GA 30332, USA
E-mail: chengzhu@gatech.edu

A. Pouya
Laboratoire Navier/CERMES, Paris-Est University,
6 & 8 Avenue Blaise Pascal, Cité Descartes,
Champs sur Marnes, 77455 Marnela Vallée Cedex 2, France
E-mail: ahmad.pouya@enpc.fr

C. Arson
School of Civil and Environmental Engineering,
Georgia Institute of Technology,
790 Atlantic Drive, Atlanta, GA 30332, USA
E-mail: chloe.arson@ce.gatech.edu

1 Introduction

A fundamental understanding of the viscous behavior of salt is crucial for the design and performance assessment of geological facilities used for the storage of hydrogen, oil and gas, as well as Compressed Air Energy Storage (CAES). Viscous deformation and damage during short-term to long-term pressurization and depressurization processes are great concerns to engineers and researchers.

Long-term creep behavior of salt is complex and depends on a number of factors (Carter and Hansen 1983). Temperature plays a key role in salt deformation around nuclear waste disposals (Senseny et al. 1992). Brine present at grain boundaries largely affects the rheology and deformation of halite polycrystals (Urai et al. 1986). Salt steady state strain rate increases as deviatoric stress increases or as confining pressure decreases (Yang et al. 1999).

Most salt constitutive models do not account for creep-induced damage, which is usually associated with the opening of microcracks or microvoids (Brace et al. 1966). In brittle solids, micro-cracks propagate along

the maximum compressive stress direction (Ashby and Hallam 1986). The same pattern of damage evolution was observed during salt creep. In order to couple visco-plastic deformation and damage into salt creep deformation law, Haupt (1991) proposed a constitutive model that accounts for damage-induced relaxation. Chan et al. (1992) extended the multimechanism deformation model proposed by Munson and Dawson (1984) in order to include creep-induced damage. Damage is defined as a density of microscopic cavities and cracks, and introduced in the visco-plastic flow rule, which allows the prediction of inelastic dilation in the transient creep regime (Chan et al. 1994). Chen et al. (1997) proposed a restrictions-based thermodynamic framework that captures the transition between secondary and tertiary creep: conservation laws are made dependent on jump functions. All of these creep-damage coupled models require a large number of constitutive parameters and do not link the macroscopic strain rates to the microscopic mechanisms that govern the behavior of halite crystals.

This paper aims to gain fundamental understanding of the microscopic mechanisms that control the transition between secondary and tertiary creep around salt caverns in typical geological storage conditions. In section 2, we explain how to model sliding mechanisms at the grain scale. In section 3, we present a micro-macro modeling approach that links salt viscous deformation and damage to elementary crystal sliding mechanisms. We use the micromechanical model to find the critical viscoplastic strain that triggers grain breakage, which we define as a damage threshold in a phenomenological model of salt visco-plastic deformation, in which a damage variable controls the transition between secondary and tertiary creep regimes (Section 4). In section 5, we present Finite Element simulations of long-term creep deformation and damage around a depressurized salt cavern.

2 Salt crystal deformation

Deformation of a salt crystal is temperature and pressure dependent. Since we focus on the CAES conditions, we choose constitutive models and parameters that are suitable for room temperature and simple compression conditions.

2.1 Kinematics

Salt rock is made of halite (NaCl) mono-crystals, all of which follow a typical face-centered cubic (FCC) structure (Fig. 1). Taking all constituents of the crystal as atoms, intra-granular dislocations would occur on planes separating the two densest grain fractions, i.e. on planes normal to the $< 1\,1\,1 >$ direction of the grain coordinate system. However, halite crystals comprise two FCC ionic sub-networks (sodium Na^+ and chloride Cl^-). Because of the electronic interaction forces between ions, the planes along which sliding requires the minimum energy input are the $\{1\,0\,1\}$ planes, as supported by a great number of experimental studies on halite crystals (Davidge and Pratt 1964; Carter and Heard 1970; Argon et al. 1972; Skrotzki and Haasen 1984; Senseny et al. 1992). Other mechanisms including cubic and octahedric systems exist, but do not contribute significantly to salt deformation at room temperature. A review of the dominant sliding mechanisms in FCC crystals can be found in (Groves and Kelly 1963; Nebozhyn et al. 2001).

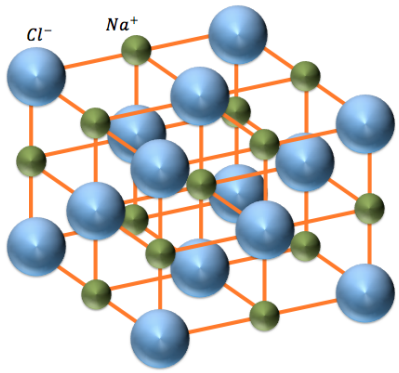

Fig. 1 Face-centered cubic (FCC) crystal structure of salt.

In the global matrix coordinate system, we note the l^{th} slip system ($\boldsymbol{a^l}$) of the mono-crystal as:

$$a^l_{ij} = \frac{n^l_i m^l_j + n^l_j m^l_i}{2}, \tag{1}$$

in which $\boldsymbol{n^l}$ is the vector normal to the l^{th} sliding plane, and $\boldsymbol{m^l}$ is the l^{th} unit sliding vector. In the local coordinate system, we can express the slip systems ($\boldsymbol{A^l}$) of the mono-crystal as follows:

$$\boldsymbol{A^l} = \boldsymbol{N^l} \,\widehat{\otimes}\, \boldsymbol{M^l}, \quad A^l_{ij} = \frac{1}{2}\left(N^l_i M^l_j + N^l_j M^l_i\right), \tag{2}$$

in which $\boldsymbol{N^l}$ is the vector normal to the l^{th} sliding plane, $\boldsymbol{M^l}$ is the l^{th} unit sliding vector, and $\widehat{\otimes}$ is the symmetric tensor product.

With the global slip system, we can write the viscoplastic strain rate ($\dot{\boldsymbol{\varepsilon}}^{vp}$) of the grain as

$$\dot{\varepsilon}^{vp}_{ij} = \sum_{l=1}^{L} \dot{\gamma}^l a^l_{ij}, \tag{3}$$

in which $\dot{\gamma}^l$ is the viscoplastic strain rate of grains subjected to the l^{th} sliding mechanism, L is the total number of active sliding mechanisms. For each halite mono-crystal, $L = 6$.

For each mono-crystal, we can relate $\left[\boldsymbol{a}^l\right]$ to the l^{th} sliding mechanism expressed in the local coordinate system, $\left[\boldsymbol{A}^l\right]$, by means of a projection tensor $[\mathbf{P}]$, which depends on the orientation of the mono crystal as

$$\left[\boldsymbol{a}^l\right] = [\boldsymbol{P}]\ \left[\boldsymbol{A}^l\right][\boldsymbol{P}]^T, \tag{4}$$

where the projection tensor $[\boldsymbol{P}]$ is decomposed as $[\boldsymbol{P}] = [\boldsymbol{P}_1][\boldsymbol{P}_2][\boldsymbol{P}_3]$, with

$$[\boldsymbol{P}_1] = \begin{bmatrix} cos\Psi & sin\Psi & 0 \\ -sin\Psi & cos\Psi & 0 \\ 0 & 0 & 1 \end{bmatrix} \tag{5}$$

$$[\boldsymbol{P}_2] = \begin{bmatrix} cos\theta & 0 & sin\theta \\ 0 & 1 & 0 \\ -sin\theta & 0 & cos\theta \end{bmatrix} \tag{6}$$

$$[\boldsymbol{P}_3] = \begin{bmatrix} cos\Phi & -sin\Phi & 0 \\ sin\Phi & cos\Phi & 0 \\ 0 & 0 & 1 \end{bmatrix}, \tag{7}$$

in which Ψ, θ, and Φ are the angles representing the orientation of the grain.

Because of the electronic interaction forces among ions, preferential sliding planes, along which sliding requires the minimum energy input, are the $\{101\}$ planes. Therefore, the vectors normal to the preferential sliding planes ($\boldsymbol{N^l}$) are:

$$\begin{aligned} \boldsymbol{N^1} &= \tfrac{1}{\sqrt{2}}(0,1,1) \quad \boldsymbol{N^2} = \tfrac{1}{\sqrt{2}}(1,0,1) \\ \boldsymbol{N^3} &= \tfrac{1}{\sqrt{2}}(-1,-1,0) \quad \boldsymbol{N^4} = \tfrac{1}{\sqrt{2}}(0,-1,1) \\ \boldsymbol{N^5} &= \tfrac{1}{\sqrt{2}}(-1,0,1) \quad \boldsymbol{N^6} = \tfrac{1}{\sqrt{2}}(-1,1,0), \end{aligned} \tag{8}$$

in which the sliding directions are respectively

$$\begin{aligned} \boldsymbol{M^1} &= -\boldsymbol{N^4} \quad \boldsymbol{M^2} = -\boldsymbol{N^5} \quad \boldsymbol{M^3} = -\boldsymbol{N^6} \\ \boldsymbol{M^4} &= -\boldsymbol{N^1} \quad \boldsymbol{M^5} = -\boldsymbol{N^2} \quad \boldsymbol{M^6} = -\boldsymbol{N^3}. \end{aligned} \tag{9}$$

Slip system $\mathbf{A}^4 = \mathbf{N}^4 \mathbin{\widehat{\otimes}} \mathbf{M}^4$ ($\mathbf{A}^5 = \mathbf{N}^5 \mathbin{\widehat{\otimes}} \mathbf{M}^5$ and $\mathbf{A}^6 = \mathbf{N}^6 \mathbin{\widehat{\otimes}} \mathbf{M}^6$, respectively) is normal to slip system $\mathbf{A}^1 = \mathbf{N}^1 \mathbin{\widehat{\otimes}} \mathbf{M}^1$ ($\mathbf{A}^2 = \mathbf{N}^2 \mathbin{\widehat{\otimes}} \mathbf{M}^2$ and $\mathbf{A}^3 = \mathbf{N}^3 \mathbin{\widehat{\otimes}} \mathbf{M}^3$, respectively). Moreover, we have

$$\mathbf{A}^1 = \mathbf{A}^2 + \mathbf{A}^3. \tag{10}$$

Therefore, the 6 sliding mechanisms of the family $\{101\} < 101 >$ provide only two linearly independent slip systems to define the viscous strain direction. Assuming that grain viscoplastic deformation is isochoric, the microscopic viscoplastic deformation tensor has five degrees of freedom. Since there are only two linearly independent slip systems for the family $\{101\} < 101 >$, slip mechanisms only provide two degrees of freedom for the microscopic viscolastic tensor. This deficit in degrees of freedom results in geometric incompatibilities between adjacent grains, which originates internal stresses in the polycrystal. In fact, single NaCl crystals cannot accommodate the deformation of their neighbors by deforming viscoplastically: elastic deformation is necessary to maintain the contact with neighboring grains of different orientations. These elastic strains generate internal stresses which can in turn lead to crack propagation within the polycrystal. These internal stresses were studied by Pouya (1991; 2000) in elastoplasticity.

2.2 Rheology

The total deformation is the sum of elastic and viscoplastic deformation as

$$\dot{\boldsymbol{\varepsilon}} = \dot{\boldsymbol{\varepsilon}}^{\boldsymbol{e}} + \dot{\boldsymbol{\varepsilon}}^{\boldsymbol{vp}}, \tag{11}$$

in which elastic strain rate $\dot{\boldsymbol{\varepsilon}}^{\boldsymbol{e}}$ is related to the stress rate, and $\dot{\boldsymbol{\varepsilon}}^{\boldsymbol{vp}}$ is the viscoplastic strain rate.

Note that contrary to previous salt plasticity models (Pouya 2000), viscoplastic models have no threshold, therefore sliding mechanisms are all active. We relate local shear stress τ^l to micro-stress $\boldsymbol{\sigma}$ by

$$\tau^l = \boldsymbol{\sigma} : \boldsymbol{a}^l. \tag{12}$$

Based on the correlations established by Wanten et al. (1996), we assume that the irreversible shear strain rate obeys a power law as

$$\dot{\gamma}^l = \gamma_0\, h^l \left|\frac{\tau^l}{\tau_0}\right|^n, \tag{13}$$

in which n and γ_0 are material constants. γ_0 is a reference strain rate and τ_0 is a reference shear stress, arbitrarily set equal to 1MPa. h^l depends on the sign of τ^l: if τ^l is positive, $h^l = 1$; if τ^l is negative, $h^l = -1$.

3 Homogenization scheme

3.1 Averaging Method

We consider the Representative Elementary Volume (REV) of salt rock as an aggregate of halite mono-crystals of various orientations. Averages computed in the space of crystal orientations form the basics of the upscaling scheme. To determine a system of coordinates in this

space, we use (X, Y, Z) to denote a system of crystallographic axes attached to the inclusion (Fig. 2). The orientation of the Z-axis is determined by two spherical coordinates (angles Ψ and θ), defined in the Cartesian coordinate system (x, y, z). Let (u, v, z) be the system obtained from (x, y, z) through rotation around the z-axis at angle Ψ. Let (U, v, Z) be the system obtained from (u, v, z) through rotation around the v-axis at angle θ. System (X, Y, Z) is obtained from system (U, v, Z) by additional "spinal" rotation around the Z-axis at angle Φ, which varies between 0 and 2π.

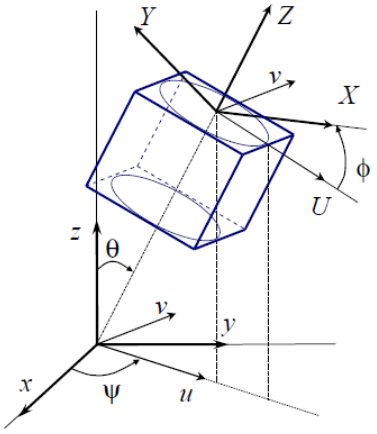

Fig. 2 Characterization of mono-crystal orientations in a spherical coordinate system.

The probability of having a Z-axis of orientation (Ψ, θ, Φ) is the product of the probability of the occurrence of solid angle Ω (measured by $d\Omega = sin\theta d\theta d\Psi$) by that of spinal rotation Φ (measured by $d\Phi$). Therefore, the density of the probability of the occurrence of grain orientation ω_1 is measured by

$$dp = p(\omega_1)d\omega_1 = p(\Psi, \theta, \Phi)\, sin\theta\, d\theta d\Psi d\Phi. \tag{14}$$

The average of a function $f(\omega_1)$ can be defined as

$$\begin{aligned}\overline{f} &= \frac{1}{\Omega_1}\int_{\Omega_1} f(\omega_1)d\omega_1 \\ &= \frac{1}{8\pi^2}\int_{\theta=0}^{\pi}\int_{\Psi=0}^{2\pi}\int_{\Phi=0}^{2\pi} f(\Psi, \theta, \Phi)\, sin\theta\, d\theta d\Psi d\Phi.\end{aligned} \tag{15}$$

All halite mono-crystals have the same FCC structure. Since the inclusion (or "grain") represents a single crystal, crystalline symmetries allow the reduction of the variation of Φ to interval $[0, \pi/2]$. Finally, changing θ to $\pi - \theta$, Ψ to $2\pi - \Psi$ and Φ to $2\pi - \Phi$ leads to the same crystallographic orientation (in which Y is replaced by $-Y$). This substitution reduces the domain of variations of θ to interval $[0, \pi/2]$. Because a uniaxial macroscopic loading test is simulated, the REV presents a symmetry around the z-axis. Therefore, Ψ can be set equal to a constant ($\Psi = 0$ is adopted in the following). As a result, in the proposed approach, the average is defined as

$$\overline{f} = \frac{2}{\pi}\int_{\theta=0}^{\pi/2}\int_{\Phi=0}^{\pi/2} f(\theta, \Phi)\, sin\theta\, d\theta d\Phi. \tag{16}$$

Using the variable change $u = cos\theta$, Eq. 16 can be rewritten as

$$\overline{f} = \frac{2}{\pi}\int_{u=0}^{1}\int_{\Phi=0}^{\pi/2} f(u, \Phi)\, du d\Phi. \tag{17}$$

We assume the same probability of occurrence for all grain orientations, that is, following a uniform probability density function. To obtain equipotent points in a discrete integration scheme, it is sufficient to divide the domain of variation of u ($[0, 1]$) into n_u intervals of central value u_i and the domain of variation of Φ ($[0, \pi/2]$) into n_Φ intervals of central value Φ_j. The average is finally computed as

$$\overline{f} = \frac{1}{N}\sum_{i,j} f(\theta_i, \Phi_j), \tag{18}$$

in which $N = n_u\, n_\Phi$ and $\theta_i = cos^{-1}(u_i)$. We adopt an isotropic distribution of grain orientations without accounting for any texture. The procedure for solid angle integration is the following: since the solid angle element reads $sin\theta\, d\theta d\Phi$, we divide the range of angle θ into 10 equipotent intervals (same variations of $cos\theta$); each of these intervals is then divided into 20 subdomains intercepted by the angle Φ. This provides 200 possible orientations for the grain (i.e., $N = 200$). Simulations with more points required longer computation time but presented similar results, which indicated that $N = 200$ was a representative number of orientations for homogenization purposes.

3.2 Inclusion-matrix model

The stresses and strains in mono-crystals depend on the macroscopic load imposed on the aggregate and on the interactions among these mono-crystals. We propose an inclusion-matrix model to account for the interactions among grains. Following a self-consistent upscaling scheme, we treat each mono-crystal as an inclusion embedded in an infinite homogeneous matrix, which represents the polycrystalline aggregate. In this model, we treat mono-crystals as spherical inclusions (Fig. 3).

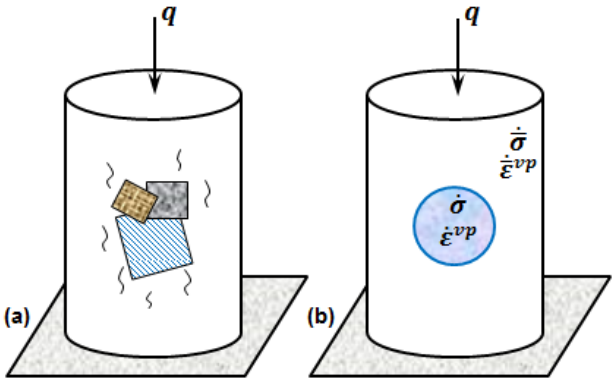

Fig. 3 Representative Elementary Volume (REV) of salt rock. (a). Monocrystal inclusions in the homogeneous matrix. (b). Schematic representation of salt mono-crystals in the inclusion-matrix model.

Microscopic stresses at the interface between two constituents reach their balance by correcting the macroscopic stress (strain, respectively) by an *eigenstress* (*eigenstrain*, respectively). We deduce aggregate REV properties (e.g., the REV stiffness matrix) from the knowledge of stress (strain, respectively) concentration tensors, which depend on the geometry of the heterogeneity present in the aggregate (Nemat-Nasser and Hori 1993).

For a homogeneous and isotropic elastic matrix, Weng (1982) extended the Kröner model proposed initially for elasto-plastic materials to viscoplastic materials as

$$\dot{\boldsymbol{\sigma}} - \dot{\overline{\boldsymbol{\sigma}}} = 2\mu(1-\beta)(\dot{\overline{\boldsymbol{\varepsilon}}}^{vp} - \dot{\boldsymbol{\varepsilon}}^{vp}), \tag{19}$$

in which $\dot{\boldsymbol{\sigma}}$ is the rate of microscopic stress and $\dot{\overline{\boldsymbol{\sigma}}}$ the rate of macroscopic stress. $\dot{\overline{\boldsymbol{\varepsilon}}}^{vp}$ and $\dot{\boldsymbol{\varepsilon}}^{vp}$ denote the macroscopic and microscopic viscoplastic strain rates, respectively (Fig. 3b). β is given by

$$\beta = \frac{2(4-5\nu)}{15(1-\nu)}, \tag{20}$$

in which ν is the Poisson's ratio of the homogenized REV.

Both the mono-crystal inclusions and the matrix follow viscoplastic laws. We adopted the viscoelastic self-consistent model of Weng, which is based on Eshelby's inclusion model. In this model, we capture the matrix-inclusion interaction with a purely elastic matrix behavior model, which implies that macroscopic viscoplasticity only stems from grain-scale viscoplastic deformation rather than grain/matrix incompatibilities. We couple the local stress in the inclusions ($\boldsymbol{\sigma}$) and the far-field stress in the matrix ($\overline{\boldsymbol{\sigma}}$) to the microscopic strain ($\boldsymbol{\varepsilon}$) and the macroscopic strain ($\overline{\boldsymbol{\varepsilon}}$) by the following relationship:

$$\boldsymbol{\sigma} - \overline{\boldsymbol{\sigma}} = -\boldsymbol{L}^{*} : (\boldsymbol{\varepsilon} - \overline{\boldsymbol{\varepsilon}}), \tag{21}$$

where $\boldsymbol{L}^{*}$ is Hill's tensor for a spherical inclusion in an isotropic matrix (Hill 1965).

In this study, we focus on damage effects coupled to the viscous deformation of the aggregate. Viscous accommodation is not accounted for, in order to better understand the effects of damage in the inclusion-matrix interaction model.

3.3 Micro-macro damage model

At the macroscopic scale, we define damage as the reduction in elastic moduli and rock strength. Tension, compression, or shear drive damage propagation at the macroscopic scale (Bobet and Einstein 1998). At the grain scale, damage triggers when one mono-crystal fails. We restrict the damage initiation at the grain scale to mode I failure, which occurs when the microscopic stress exceeds the tensile strength σ_T of salt mono-crystals. In this model, we represent crack propagation at the grain-matrix interface or inside the grain by the breakage of the whole grain. If the major principal local stress of a grain exceeds σ_T, the grain is breaking. Damage propagates when subsequent stress redistribution and further loading increase micro-stress in other grains to the tensile limit. We denote the number of unbroken grains as N_g, the number of broken grains N_b, and the total number of grains in the REV N (with $N = n_u\, n_\Phi$, the number of mono-crystal orientations studied in the REV). We reckon that this assumption is crude, however modeling microscopic damage along the grain interfaces cannot be done in the framework of the inclusion-matrix model used here and falls beyond the scope of this work.

The Voigt estimate for the elastic matrix yields the effective bulk modulus ($\widetilde{\kappa}$) and shear modulus ($\widetilde{\mu}$) as

$$\begin{aligned} \widetilde{\kappa} &= \tfrac{N_g}{N}\kappa = \tfrac{N-N_b}{N}\kappa = (1-D_m)\kappa \\ \widetilde{\mu} &= \tfrac{N_g}{N}\mu = \tfrac{N-N_b}{N}\mu = (1-D_m)\mu, \end{aligned} \tag{22}$$

in which D_m, defined as $D_m = N_b/N = 1 - N_g/N$, is the macroscopic damage variable obtained from the micro-macro analysis. From the expressions of the damaged bulk and shear moduli in Eq. 22, we realize that Poisson's ratio does not change upon grain breakage: $\widetilde{\nu} = \nu$. The proposed micro-macro modeling approach combines Hill's scheme (Hill 1965) for the rate-independent non-linear elastic matrix behavior (to represent the inclusion matrix interaction), and a brittle constitutive law for the grains subject to breakage (to represent damage). We calculate Hill's constraint tensor for the damaged matrix. As a result, in the present work, the inclusion-matrix interaction model accounts for brittle grain breakage, but it does not capture the "viscous

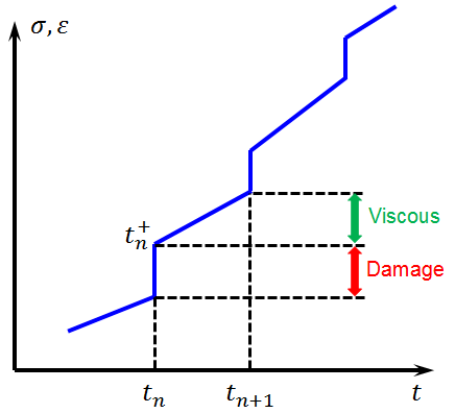

Fig. 4 Computational method: decomposition of each time step into damage and viscous phases.

accommodation" because of the viscous deformation of the matrix. As mentioned earlier we adopt this simplification because the focus of this study is macroscopic fatigue behavior induced by creep or cyclic loading.

For each macroscopic stress loading increment $\delta q(t)$ applied between times t_n and t_{n+1}, we update the macroscopic and microscopic variables in two steps, as illustrated in Fig. 4:

1. The "damage phase" ($t_n \sim t_n^+$) accounts for instantaneous variations because of grain breakage at time t_n. We denote these variations as $\delta\boldsymbol{\sigma}$, $\delta\boldsymbol{\varepsilon}$, $\delta\overline{\boldsymbol{\sigma}}$, $\delta\overline{\boldsymbol{\varepsilon}}$.
2. The "viscous phase" ($t_n^+ \sim t_{n+1}$) accounts for time-dependent variations because of viscous deformation on the time interval $\Delta_n t = t_{n+1} - t_n$. We denote these variations as $\dot{\sigma}\Delta_n t$, $\dot{\varepsilon}\Delta_n t$, $\dot{\overline{\boldsymbol{\sigma}}}\Delta_n t$, $\dot{\overline{\boldsymbol{\varepsilon}}}\Delta_n t$.

At each stress increment (i.e., time step), we check the grain breakage criterion at the beginning of the damage phase ($t = t_n$) and then sort grains into three categories, depending on the stress state of the mono-crystal:

- The grain is non-broken if the maximum principal microscopic stress is less than the mono-crystal tensile strength σ_T.
- The grain is breaking if the maximum principal microscopic stress exceeds the mono-crystal tensile strength σ_T during the current loading increment.
- The grain is broken if the mono-crystal has already been broken in a previous loading increment.

Initially at $t = t_n$, we calculate the damaged elastic moduli from Eq. 22, in which N_b accounts for both breaking and broken grains. For all three types of grains, the Hill's formula (Eq. 21) governs the inclusion-matrix interaction. Grain breakage results in a redistribution of micro-stresses: when breaking grains actually fail, non-broken grains become subjected to microscopic stresses of higher magnitude. At the beginning of the viscous phase (at $t = t_n^+$), we update resulting micro-stresses using the equations for the sliding mechanisms. Note that the redistribution of micro-stresses because of grain breakage (at $t = t_n^+$) can result in tensile stresses that exceed the tensile strength in some of the non-broken grains. We count those grains subjected to higher stresses than the tensile strength as non-broken during the viscous phase of the loading (between $t = t_n^+$ and $t = t_{n+1}$). We will check the status of the grains and update them at the beginning of the damage phase of the following loading increment (at $t = t_{n+1}$). As the damage and viscoplastic updates are step dependent, we simulate stress paths with a high number of increments to ensure that there is no significant numerical difference between results obtained when updates are done at step n or step $n+1$. Sufficiently small time increments are used, so that the numerical solution tends to the real solution.

Simulation of the creep of salt polycrystals using this model showed that creep deformation obeyed a power law in stress, and that the onset of the tertiary creep is exactly related to the initiation of damage (Pouya et al. 2015). This result makes it possible to identify the onset of damage by analysing experimental creep curves. The procedure to calibrate the transition between secondary and tertiary creep phases is explained in Section 4 below.

4 Phenomenological modeling framework

To study salt viscous damage at the field scale, we propose a phenomenological model of visco-plastic deformation that captures the transition between secondary and tertiary creep regimes. In the following, we define this transition with a micro-macro damage criterion. During the secondary creep regime, the visco-plastic deformation is the result of grain-scale sliding mechanisms. During tertiary creep, the strain rate increases with damage as the consequence of grain breakage. We use Norton-Hoff law for secondary creep (Carter and Hansen 1983):

$$\dot{\boldsymbol{\varepsilon}}_{ss}^{vp} = \frac{3}{2} A \cdot exp(-\frac{Q}{RT})(\frac{\sigma_e}{\sigma_0})^{n_1} \frac{1}{\sigma_e}\boldsymbol{s}, \tag{23}$$

in which A and n_1 are material constants, Q is the activation energy for the slip mechanism, R is the universal gas constant, T is the absolute temperature, $\boldsymbol{s}$ is the deviatoric stress tensor, σ_0 is a reference stress, arbitrarily set equal to 1MPa, $\sigma_e = \sqrt{3J_2}$ is the equivalent von Mises stress, and $J_2 = \frac{s_{ij}s_{ij}}{2}$ is the second deviatoric stress invariant. This relation is equivalent to the macroscopic viscoplastic law proposed in our previous

study (Zhu et al. 2015). Experiments conducted at various temperatures led to similar empirical power laws (Heard 1972; Handin et al. 1986).

For the case of uniaxial creep, according to Eq. 23, we have

$$\dot{\varepsilon}_a^{vp} = A \cdot exp(-\frac{Q}{RT})(\frac{\sigma_e}{\sigma_0})^{n_1}, \tag{24}$$

in which σ_e is the uniaxial stress.

Micro-stresses increase with macroscopic viscoplastic deformation, which may cause grain breakage if grain tensile strength is exceeded. The consequent redistribution of microstresses leads to higher local stress concentrations, which further accelerate viscoplastic deformation and damage progagation. This phenomenon is known as tertiary creep (Fig. 5).

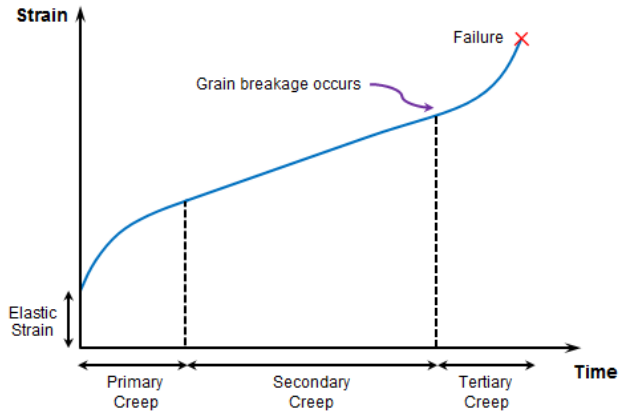

Fig. 5 Complete creep curve. Tertiary creep phase initiates when first grain breakage occurs.

As explained here-above, according to micromechanical analysis, we related the onset of the tertiary creep to the damage initiation, i.e., tertiary creep is triggered by grain breakage. In the micro-macro modeling framework presented above, we accounted for the consequent mechanical macroscopic damage (D_m) by scaling the elastic properties by the the fraction of non-broken grains in the REV. In the following, we denoted the damage variable in the phenomenological model as D_M to account for the change of viscoplastic strain rate induced by grain breakage - which we modeled as the opening of microcracks and microvoids (Hutchinson 1983; Ashby and Hallam 1986). The tertiary creep deformation law is similar to the secondary creep law (Leckie and Hayhurst 1974):

$$\dot{\boldsymbol{\varepsilon}}_{ts}^{vp} = \frac{3}{2} B \cdot exp(-\frac{Q}{RT})[\frac{\sigma_e/(1-D_M)}{\sigma_0}]^{n_2} \frac{1}{\sigma_e} \boldsymbol{s}, \tag{25}$$

in which B and n_2 are material constants. $\frac{\sigma_e}{1-D_M}$ is the effective stress. The damage variable D_M also contributes to the degradation of material stiffness as

$$\boldsymbol{C_D} = (1 - D_M)\boldsymbol{C_0}, \tag{26}$$

in which $\boldsymbol{C_D}$ is the stiffness of the damaged material, $\boldsymbol{C_0}$ is the initial stiffness of the undamage material. For uniaxial creep, according to Eq. 25, we have

$$\dot{\varepsilon}_a^{vp} = B \cdot exp(-\frac{Q}{RT})[\frac{\sigma_e/(1-D_M)}{\sigma_0}]^{n_2}, \tag{27}$$

in which σ_e takes the value of the uniaxial axial stress.

We compare two damage evolution laws. The first law (noted as damage evolution law 1), initially proposed for metallic materials (Hayhurst et al. 1984), depends on both the current damage and stress states as

$$\dot{D}_M = \frac{C\sigma_e^{\xi}}{(1-D_M)^{\varphi}}, \tag{28}$$

in which C, ξ, and φ are material constants governing the damage accumulation during the tertiary creep phase. The second damage evolution law (noted as damage evolution law 2), which depends on the current viscoplastic deformation state only, was successfully employed to model concrete (Mazars 1984) and interfaces in cementitious materials (Jefferson 1998). We assume that damage remains equal to zero up to a critical viscoplastic deformation ε_0^{vp}, and then increases exponentially with deformation as

$$D_M = 1 - e^{-\frac{\varepsilon^{vp} - \varepsilon_0^{vp}}{\varkappa \varepsilon_0^{vp}}}, \tag{29}$$

As a result, the rate of damage is expressed as:

$$\dot{D}_M = \frac{1}{\varkappa \varepsilon_0^{vp}} ||\dot{\boldsymbol{\varepsilon}}^{vp}|| e^{-\frac{\varepsilon^{vp} - \varepsilon_0}{\varkappa \varepsilon_0^{vp}}}, \tag{30}$$

in which ε_0^{vp} is the critical viscoplastic strain at the onset of tertiary creep state. $\varkappa$ is a damage parameter which measures the ductility of the material: the larger the value of $\varkappa$, the more ductile the material. $||\dot{\boldsymbol{\varepsilon}}^{vp}|| = \sqrt{\frac{2}{3}\dot{\varepsilon}_{ij}^{vp}\dot{\varepsilon}_{ij}^{vp}}$ is the equivalent von Mises strain.

We implemented the micro-macro model presented in Sections 2 and 3 in MATLAB in order to study salt viscous damage at the material point. We simulated creep tests under various axial stresses, and determined the critical viscoplastic strain as the cumulated viscoplastic strain reached at the first occurance of grain breakage. In Fig. 6, the onset of tertiary creep (cross symbol) is indicated by the point where the viscoplastic deformation predicted in the absence of grain breakage (non-damage model) separates from the one predicted with the consideration of grain breakage (damage model).

We adopt the microstress mapping method introduced by Pouya (2000) for displaying the distribution

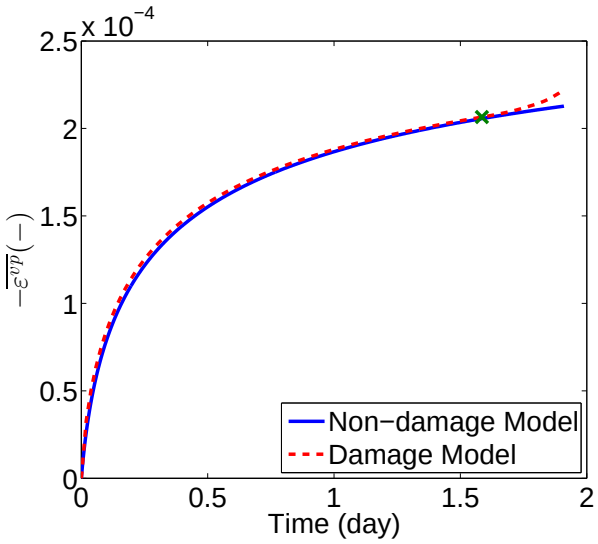

Fig. 6 Evolution of macroscopic viscoplastic strain during the long-term creep test with 7 MPa creep load.

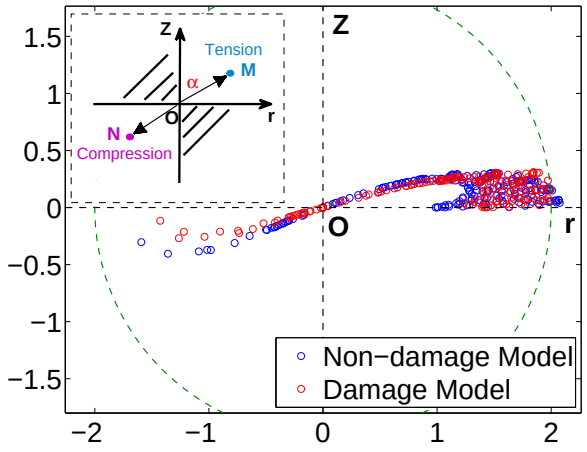

Fig. 7 Microstress mapping of all grains at the end of the long-term creep test with 7 MPa creep load. We adopt the rock mechanics sign convention with tension counted as positive.

of microstresses in grains. Vector σ_i represents the principal stresses of each grain. v_i is a unit vector indicating the i^{th} microstress eigenvector and σ_i is a scalar indicating the i^{th} microstress eigenvalue. We adopt the rock mechanic sign convention with tension counted as positive. In a $r-z$ plane, vector $\overrightarrow{OM}$ refers to a tensile principal stress ($r>0$, $z>0$) and vector $\overrightarrow{ON}$ a compressive principal stress ($r<0$, $z<0$). α measures the angle between the compression axis z and the direction of principal microstress. The microstress map in Fig. 7 follows that convention, and shows the sign and the magnitude of the principal microstresses, as well as the angle between the compression axis and principal microstresses for each grain orientation studied in the REV. In the absence of grain breakage (non-damage model), micro-stress in the grains can exceed 2 MPa. When grain breakage is accounted for (damage model), grains break as soon as micro-stress exceeds 2 MPa, which results in grains that support zero stress.

We determined the critical viscoplastic deformation for creep tests under various axial stresses, and established a relationship between critical viscoplastic strain ε_c^{vp} and creep load σ_c at a material point - for both short-term and long-term creep tests. Fig. 8 shows the resulting damage threshold, which is similar to a yield surface.

Note that the damage criterion obtained with short-term creep parameters is similar to that obtained with long-term creep parameters, which confirms that the occurrence of damage depends on the cumulated viscoplastic strain - as opposed to the viscoplastic strain rate. In addition, our modeling approach is in agreement with the work presented by Kranz and Scholz

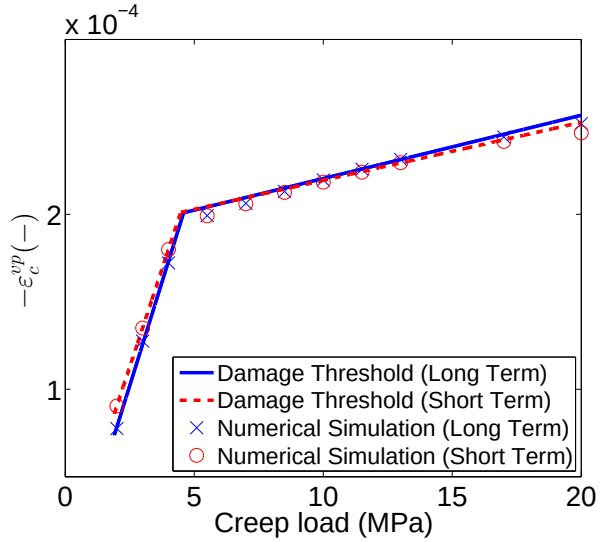

Fig. 8 Damage criterion determined from micromechanical model (long term and short term).

(1977), according to which the onset of tertiary creep should not depend on stress (but rather, on viscoplastic strain).

Since this study focuses on the long-term behavior of salt cavern subjected to creep load, we used the damage criterion based on long-term creep datasets for the following simulations. The damage threshold takes a bilinear form. Linear fitting provides:

$$\varepsilon_c^{vp} = 5\times10^{-5}\sigma_c - 2\times10^{-5} \qquad (2\le\sigma_c\le 4.78) \quad (31)$$

$$\varepsilon_c^{vp} = 4\times10^{-6}\sigma_c + 2\times10^{-4} \qquad (\sigma_c > 4.78) \quad (32)$$

When σ_c is less than 2 MPa, we assume that microstress remains below 2 MPa in all grains, and therefore, that

grain breakage does not occur (i.e., the material remains in the secondary creep regime at the macroscopic scale).

5 Numerical Simulation

5.1 Model calibration

In a previous study (Zhu et al. 2015), we calibrated material constants A and n_1 against experimental results from steady state creep for both short-term and long-term tests. In the following, we calibrate tertiary creep constitutive paramters. For damage evolution law 1, these are B, n_2, C, ξ, and φ; For damage evolution law 2, these are B, n_2, and $\varkappa$. At the transition between secondary and tertiary creep, when $D_M = 0$, we have:

$$A \cdot exp(-\frac{Q}{RT})(\frac{\sigma_e}{\sigma_0})^{n_1} = B \cdot exp(-\frac{Q}{RT})(\frac{\sigma_e}{\sigma_0})^{n_2}. \qquad (33)$$

In addition, the creep deformation curve should fit experimental data. For consistency, we use the experimental data obtained from the same salt rock as in the calibration done in the secondary creep regime (Fuenkajorn and Phueakphum 2010). Tests are carried out at room temperature ($T = 295K$). The activation energy Q for cross-slip in pure alkali halides is $1.538 \times 10^4\ J \cdot mol^{-1}$ (Senseny et al. 1992). The universal gas constant R is $8.314\ J \cdot mol^{-1} \cdot K^{-1}$.

For short term creep, we obtained $A = B$ and $n_1 = n_2$. After damage initiation, the viscoplastic strain rate kept its value of $6.89 \times 10^{-2}\ day^{-1}$. We used the tertiary creep strain rate to fit the parameters involved in the damage evolution laws (Fig. 9).

We also calibrated our model against long term creep datasets (Fuenkajorn and Phueakphum 2010). The tertiary parameters B and n_2 were different from the secondary parameters A and n_1 (Fig. 10). The resulting strain rate for long term steady state creep is 5.61×10^{-4} day^{-1}. Although some deviation exists between experimental data and theoretical model, the trend is well captured by both damage models.

We verified our calibrated model against independent experimental datasets. For short term creep, we used the creep curve of another type of salt rock (Yang et al. 1999) (complete creep curve, including secondary and tertiary creep regimes). The steady state viscoplastic strain rate using calibrated parametersl is $1.72 \times 10^{-2}\ day^{-1}$, same as the reported experimental result. Damage evolution in salt rock depends on its microstructure and defects, which varies greatly among different types of salt rocks. So while keeping other parameters unchanged, we had to do an additional calibration of the two damage parameters: $C = 0.18$ and $\varkappa = 41$.

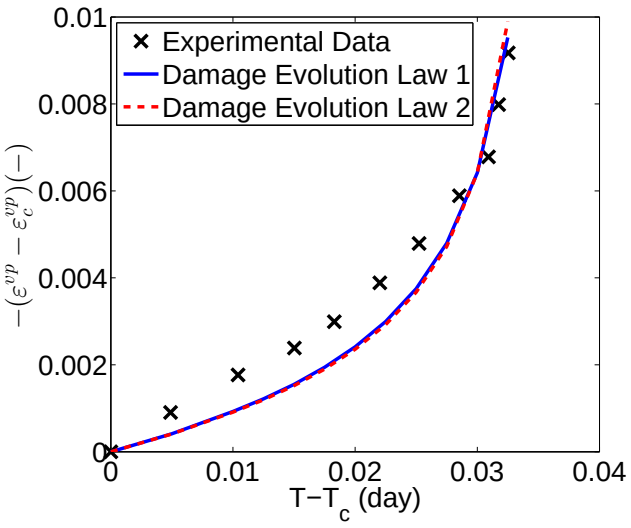

Fig. 9 Calibration of short-term parameters for the tertiary creep phase. We obtain the experimental data from the short-term creep test with the creep load 30 MPa (Fuenkajorn and Phueakphum 2010). T_c and ε_c^{vp} are the time and the critical viscoplastic strain at the onset of the tertiary phase, respectively.

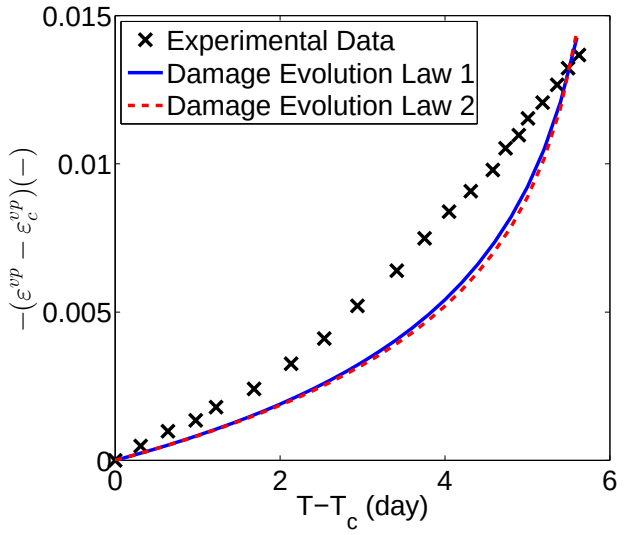

Fig. 10 Calibration of long-term parameters for the tertiary creep phase. We obtain the experimental data from the short-term creep test with the creep load 12.6 MPa (Fuenkajorn and Phueakphum 2010). T_c and ε_c^{vp} are the time and the critical viscoplastic strain at the onset of the tertiary phase, respectively.

Tables 1 and 2 summarize all calibrated parameters, for both damage evolution laws. As expected, the values of A and B for long-term creep are significantly smaller than those obtained for short term creep. The value of $\varkappa$ is larger for long-term creep - as the material becomes more ductile. Note that the proposed model is able to capture the transition between secondary and tertiary creep with an input of 8 constitutive parameters.

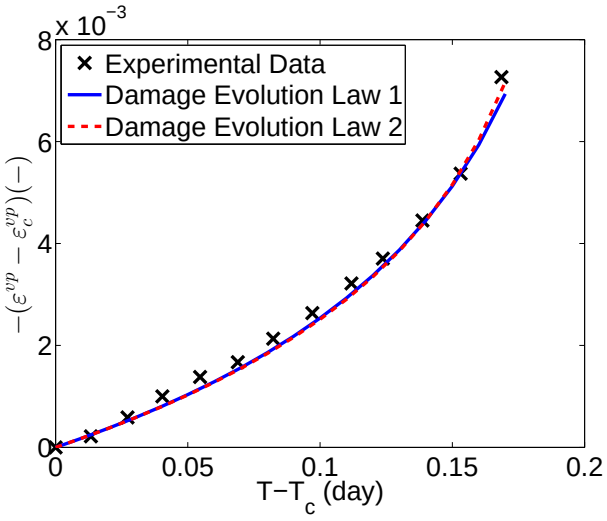

Fig. 11 Verification of short-term parameters for the tertiary creep phase. We obtain the experimental data from the short-term creep test with the creep load 21.5 MPa (Yang et al. 1999). T_c and ε_c^{vp} are the time and the critical viscoplastic strain at the onset of the tertiary phase, respectively.

Table 1 Model parameters calibrated for damage evolution law 1 based on the experimental data (Fuenkajorn and Phueakphum 2010).

short term			
A (day^{-1})	n_1 (-)	B (day^{-1})	n_2 (-)
1.88×10^{-4}	3.58	1.88×10^{-4}	3.58
C (-)	ξ (-)	φ (-)	
0.915	0.7	2.05	
long term			
A (day^{-1})	n_1 (-)	B (day^{-1})	n_2 (-)
1.06×10^{-5}	4.04	1.00×10^{-8}	6.9
C (-)	ξ (-)	φ (-)	
0.0037	0.8	4.92	

Table 2 Model parameters calibrated for damage evolution law 2 based on the experimental data (Fuenkajorn and Phueakphum 2010).

short term				
A (day^{-1})	n_1 (-)	B (day^{-1})	n_2	$\varkappa$ (-)
1.88×10^{-4}	3.58	1.88×10^{-4}	3.58	23
long term				
A (day^{-1})	n_1 (-)	B (day^{-1})	n_2	$\varkappa$ (-)
1.06×10^{-5}	4.04	1.00×10^{-8}	6.9	115

5.2 Finite element simulations

We implemented the phenomenological models into POROFIS, a Finite Element Method (FEM)-based program written in Fortran, which was developed to model coupled flow and deformation in porous fractured media (Pouya 2015). In POROFIS, we update the rock stiffness at each time increment and, in this way, we account for the damage effect on the stress field around the cavern.

We simulated the depressurization of an axisymmetric salt cavern of irregular shape (Fig. 12), which consists of both convex and concave regions and is similar to that of the Eminence salt dome site (Warren 2006). The depth and height of the cavern were 850m, and 100m, respectively. The salt formation had a unit weight of $\gamma = 0.02\ MN/m^3$, a Young's modulus of 23 GPa and a Poisson's ratio of 0.3 (Fuenkajorn and Phueakphum 2010). In the FEM analysis, we extracted a $500m$ by $500m$ domain close to the salt cavern (Fig. 12). In order to account for the overburden, we applied a vertical stress of $P_V = \gamma z = 12$ MPa at the top boundary. To achieve a homogeneous stress field and apply an in-situ level storage pressure, we applied a 12 MPa lateral stress P_H and a 12 MPa initial storage pressure P_A in the cavern. The vertical displacement was fixed at the bottom of the domain and the radial displacement fixed at the left side of the domain (axis of symmetry). We carried out the FEM simulations with both damage evolution laws and simulated a depressurization process under typical CAES conditions, in three stages:

- In stage 1 (steady state, time-independent), we applied the initial stresses.
- In stage 2 (transient state, time-dependent), within one time step, we reduced the cavern pressure from 12 MPa to 8 MPa - which is in the same order of magnitude as the stresses encountered in CAES (Ibrahim et al. 2008).
- In stage 3 (transient state, time-dependent), we maintained a stress of 8 MPa at the cavity wall for a long time (360 days), in order to reach a tertiary creep phase.

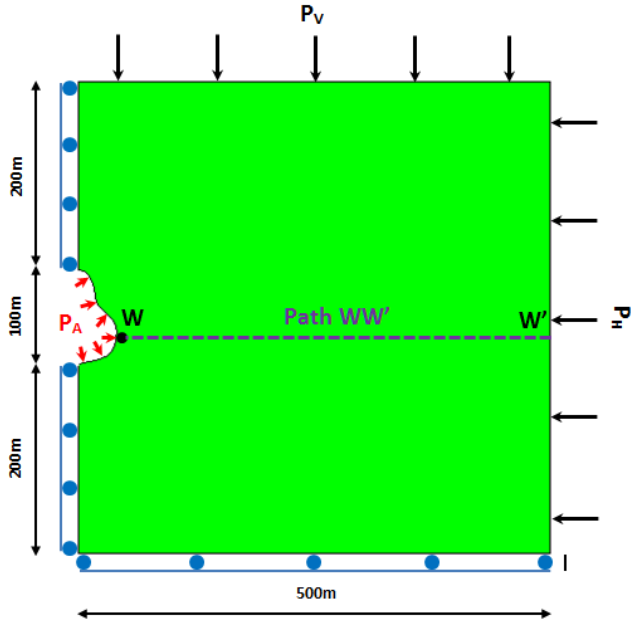

Fig. 12 Geometry and boundary conditions of a typical salt cavern studied in POROFIS. Element W is the tracing element. Maximum width of the cavern is 40m at element W.

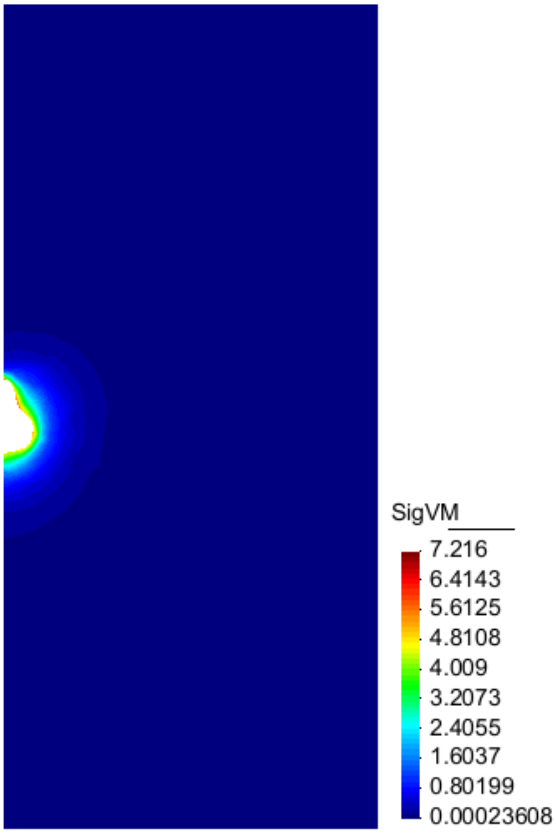

Fig. 13 Equivalent stress distribution at the end of stage 2 using a $1100m \times 500m$ domain.

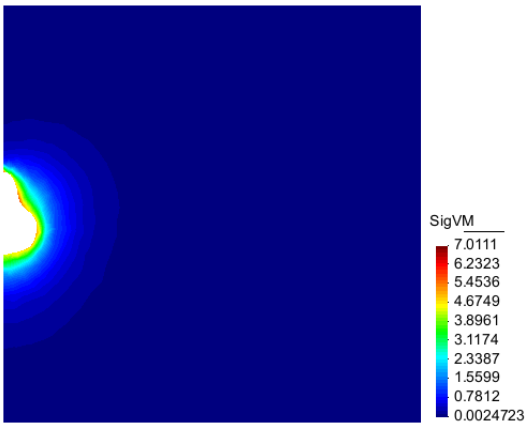

Fig. 14 Equivalent stress distribution at the end of stage 2 using a $500m \times 500m$ domain.

We simulated the salt cavern depressurization by adopting a larger domain ($1100m$ height by $500m$ width for a $100m$-high cavern) in order to check the boundary effect. At the end of stage 2, both models provide the same equivalent stress distributions, with less than 3% difference (Figs. 13 and 14). The zones of stress concentration are also similar. Comparison of other results such as the distribution of various stress components further indicates that the discrepancy is within the acceptable range of 3%. Therefore, in the following analysis, to save computational time, we used the smaller domain shown in Fig. 12. Note that results are reliable close to the cavern while relatively larger deviations exist at the far-field.

At the end of the first stage, the damage variable D_M is zero for all elements. The stress distribution is homogeneous. The resulting equivalent von Mises stress σ_e is close to zero all over the domain.

At the end of the second stage, after the depressurization in the cavern, we obtain extreme stresses around the cavern. The equivalent stress concentrates at the vicinity of the cavern, with the highest values appearing at specific locations including the roof, the most convex and concave parts (Fig. 14). This reveals the significant influence of the irregular shape of the cavern on the stress distribution surrounding the cavern. Figs. 15 and 16 show the distribution of stress components S_{rr} and S_{zz} around the cavern after stage 2.

Before the simulation reaches the end of the third stage, as a result of the stress dependence in the damage evolution law 1 (Eq. 28), damage increases rapidly in the element with the highest stress intensity (Fig. 17). Because the damage is so concentrated, it evolves very fast and does not propagate in the other elements. Therefore, damage evolution law 2 (Eq. 30) is more approriate for the long-term creep test simulation. Using damage

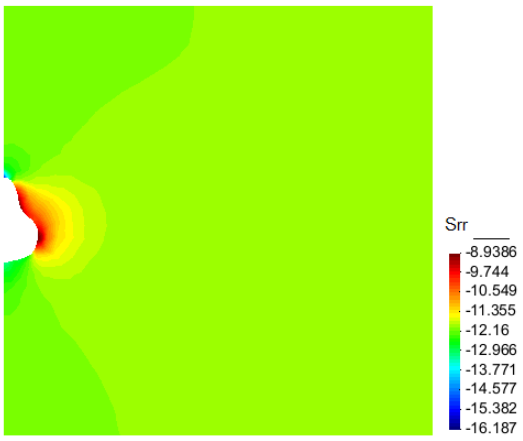

Fig. 15 Radial stress distribution at the end of stage 2.

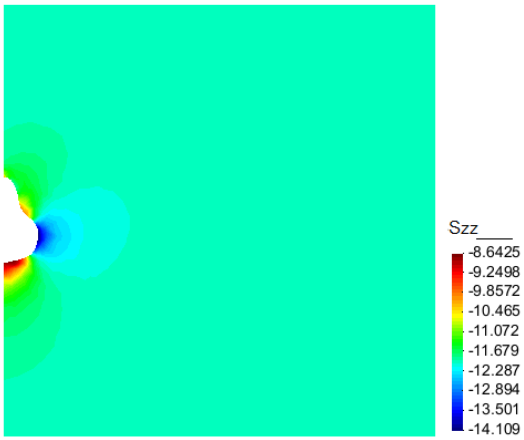

Fig. 16 Vertical stress distribution at the end of stage 2.

evolution law 2, we obtained the distribution of equivalent stress around the cavern after 360 days (Fig. 18).

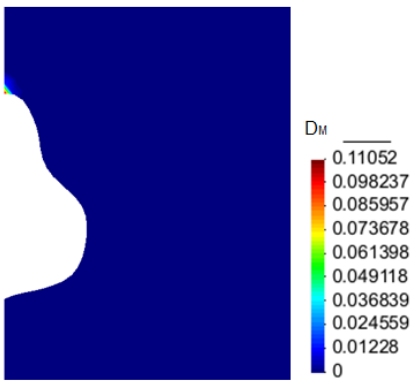

Fig. 17 Damage distribution at the end of stage 3, using damage evolution law 1 (Eq. 28). Only roof elements are damaged in this magnified image.

As expected, damage predicted with damage evolution law 2 reaches its highest value at the roof. We

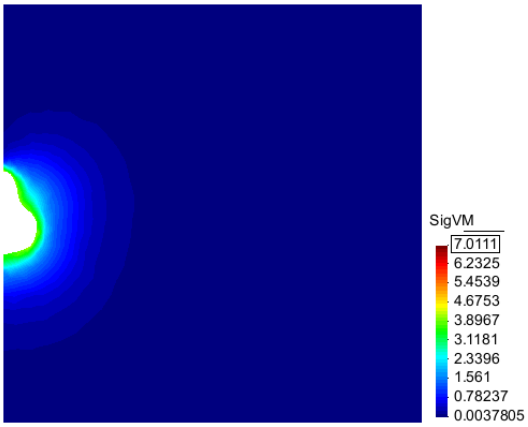

Fig. 18 Equivalent stress distribution at the end of stage 3. We use the same scale of color bar as in Figure 14.

can observe that in addition to the roof, damage tends to accumulate faster at the most convex and concave parts. The damage evolution governed by Eq. 30 is more appropriate and allows the observation of the progressive damage accumulation in all elements surrounding the cavern. Overall, the cavern does not undergo severe damage for the particular geometry and boundary conditions adopted in this problem. But as a result of viscoplastic deformation, salt caverns with complex geometries may be subjected to various types of failure such as rock fall (Djakeun 2014). Irreversible strain evolves around the cavern because of the creep load induced by internal pressure (Fig. 20). The distribution of irreversible strain matches with the distribution of damage.

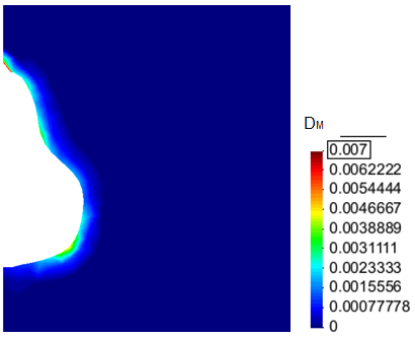

Fig. 19 Damage distribution at the end of stage 3, using damage evolution law 2. The damage variable of the roof element reaches 0.02, but we set the maximum value of the color bar to 0.007 in order to highlight the distribution of damage around the cavern.

Fig. 21 compares the stress distribution at the end of stage 2 and at the end of stage 3 along path WW' (refer to Fig. 12). Both radial and vertical stress components decrease during the creep process. This phenomenon

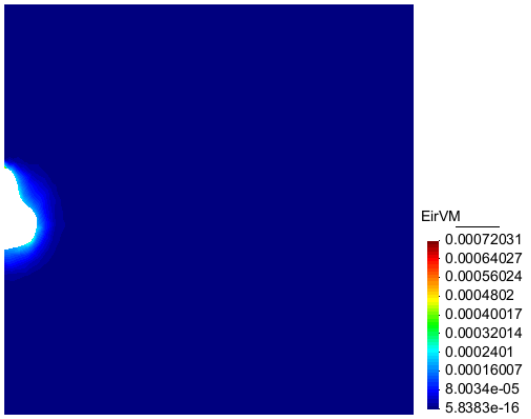

Fig. 20 Irreversible equivalent strain at the end of stage 3.

corresponds to the stress relaxation that follows the initiation of damage. The distribution of equivalent stress along WW' confirms this phenomenon (Fig. 22). The equivalent stress drops at the cavern wall whereas it remains almost unchanged in the far field.

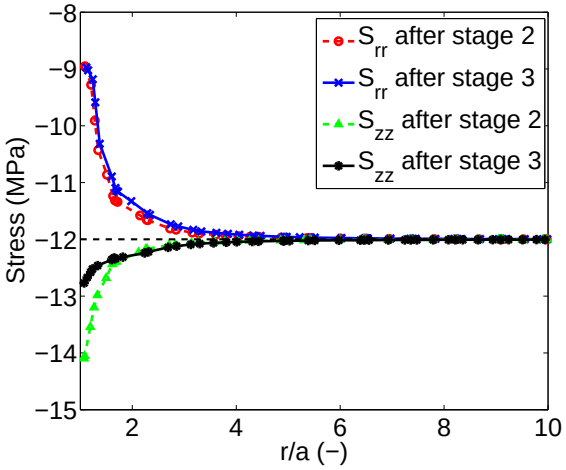

Fig. 21 Radial and vertical stress distribution along path WW' at the end of stages 2 and 3.

We tracked one element (element W in Fig. 12) at the cavern wall. We plotted the evolution of the equivalent stress in Fig. 23. Even though the pressure applied at the cavern wall is constant during stage 3, the equivalent stress decreases over time, as a result of stress relaxation induced by damage. Because of the bilinear relationship between critical viscoplastic strain and the equivalent stress, the evolution of the critical strain follows the evolution of the equivalent stress (Fig. 24). The evolution of damage in element W (Fig. 25) follows that of the viscoplastic equivalent strain, which can exceed the critical viscoplastic strain in this simulation.

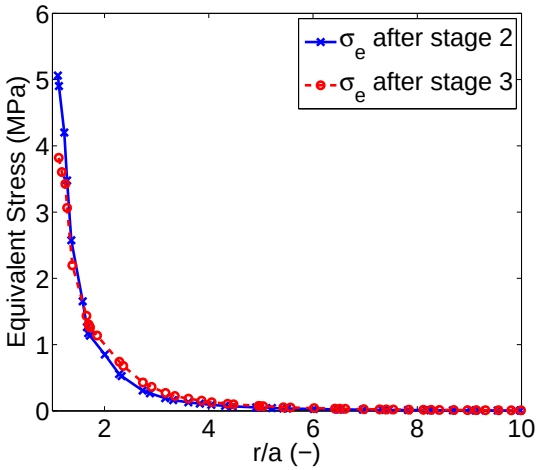

Fig. 22 Equivalent stress distribution along path WW' at the end of stages 2 and 3.

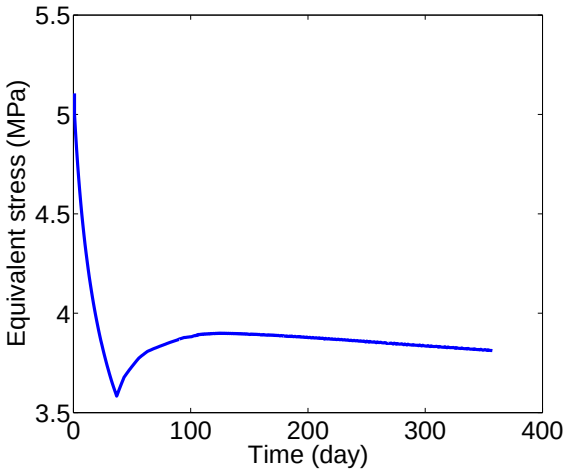

Fig. 23 Evolution of equivalent stress of element W.

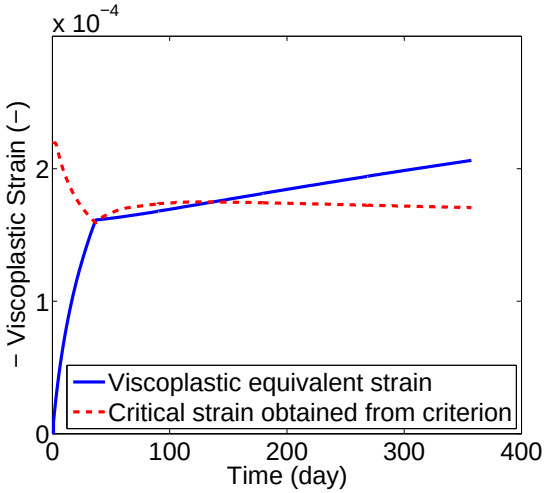

Fig. 24 Evolution of equivalent viscoplastic strain of element W.

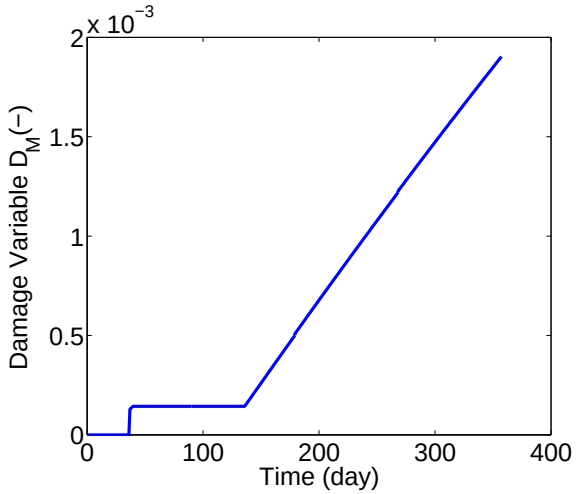

Fig. 25 Evolution of damage variable of element W.

6 Conclusions

We used a self-consistent inclusion-matrix model to homogenize the visco-plastic deformation of halite polycrystals. We introduced a scalar measure of damage in the model, defined as the number of broken grains by the total number of grains in the Representative Elementary Volume, which is defined as a polycrystal containing 200 uniformly distributed halite crystal orientations. A grain (i.e. a crystal of a given representative orientation) is assumed to break when microscopic stress exceeds halite tensile strength. We calibrated and verified the model against published experimental data obtained during creep tests, which allowed us to predict salt visco-plastic deformation during secondary creep (before grain breakage) and tertiary creep (after grain breakage), and to show that the onset of tertiary creep is related to the grain damage. We used this micro-macro modeling framework to simulate creep tests under various axial stresses, which gave us the critical visco-plastic strain at which grain breakage (i.e. tertiary creep) is expected to occur. The macroscopic damage threshold, plotted in the visco-plastic strain/stress space, is a bilinear function. The comparison of the simulation results for short-term and long-term creep indicate that the initiation of tertiary creep is a function of stress and accumulated viscoplastic strain.

In order to predict stress concentrations and damage around salt caverns used for Compressed Air energy Storage (CAES), we implemented a phenomenological model of visco-plastic deformation with damage into the Finite Element Method (FEM) program POROFIS. The tertiary creep law is similar to the secondary creep law, except that the deformation rate depends on a phenomenological damage variable. The transition between secondary and tertiary creep laws was governed by the bilinear damage threshold that we had determined by our micro-macro approach. We modeled a 850m-deep salt cavern of irregular shape, in axis-symmetric conditions. We compared two phenomenological damage evolution laws. Simulations of cavern depressurization with the stress-dependent damage evolution law provided concentrated damage at the crown, which led to numerical challenges. By contrast, the strain-dependent damage evolution law allowed capturing the formation of a damaged zone around the cavity.

Although phenomenological deformation laws are desirable for FEM implementation, the knowledge of the dominating halite crystal deformation mechanisms is critical to understand salt rock macroscopic creep rates observed around caverns and to predict the transition between secondary and tertiary creep. More work is needed to link grain breakage to the phenomenological damage variable used in Continuum Damage Mechanics to predict the reduction of elastic moduli.

Acknowledgements Financial support for this research was provided by the School of Civil and Environmental Engineering at the Georgia Institute of Technology, and by the National Science Foundation (Grant No. CMMI-1362004/1361996).

References

Argon A, Nigam A, Padawer G (1972) Plastic deformation and strain hardening in pure nacl at low temperatures. Philosophical Magazine 25(5):1095–1118

Ashby M, Hallam S (1986) The failure of brittle solids containing small cracks under compressive stress states. Acta Metallurgica 34(3):497 – 510

Bobet A, Einstein H (1998) Fracture coalescence in rock-type materials under uniaxial and biaxial compression. Int J Rock Mech Min Sci 35(7):863–888

Brace WF, Paulding BW, Scholz C (1966) Dilatancy in the fracture of crystalline rocks. J Geophys Res 71(16):3939–3953

Carter NL, Hansen FD (1983) Creep of rock salt. Tectonophysics 92(4):275–333

Carter NL, Heard HC (1970) Temperature and rate dependent deformation of halite. American Journal of Science 269(3):193–249

Chan K, Brodsky N, Fossum A, Bodner S, Munson D (1994) Damage-induced nonassociated inelastic flow in rock salt. Int J Plast 10(6):623–642

Chan KS, Bodner SR, Fossum AF, Munson DE (1992) A constitutive model for inelastic flow and damage evolution in solids under triaxial compression. Mech Mater 14(1):1–14

Chen Z, Wang ML, Lu T (1997) Study of tertiary creep of rock salt. J Eng Mech 123(1):77–82

Davidge R, Pratt P (1964) Plastic deformation and work-hardening in nacl. physica status solidi (b) 6(3):759–776

Djakeun HD (2014) Stabilite mecanique d'une cavite saline soumise a des variations rapides de pression. PhD thesis, Ecole Polytechnique

Fuenkajorn K, Phueakphum D (2010) Effects of cyclic loading on mechanical properties of maha sarakham salt. Eng Geol 112(1):43–52

Groves G, Kelly A (1963) Independent slip systems in crystals. Philosophical Magazine 8(89):877–887

Handin J, Russell JE, Carter NL (1986) Experimental deformation of rocksalt. American Geophysical Union Geophysical Monograph Series

Haupt M (1991) A constitutive law for rock salt based on creep and relaxation tests. Rock Mech Rock Eng 24(4):179–206

Hayhurst DR, Dimmer PR, Morrison CJ (1984) Development of continuum damage mechanics in the creep rupture of notched bars. Philosophical Transactions of the Royal Society of London, Series A, Math Phys Sci 311(1516):103–129

Heard HC (1972) Steady-State Flow in Polycrystalline Halite at Pressure of 2 Kilobars, vol 16, American Geophysical Union, pp 191–209

Hill R (1965) Continuum micro-mechanics of elastoplastic polycrystals. J Mech Phys Solids 13(2):89–101

Hutchinson J (1983) Constitutive behavior and crack tip fields for materials undergoing creep-constrained grain boundary cavitation. Acta Metallurgica 31(7):1079 – 1088

Ibrahim H, Ilinca A, Perron J (2008) Energy storage systems - characteristics and comparisons. Renewable and Sustainable Energy Reviews 12(5):1221–1250

Jefferson AD (1998) Plastic-damage model for interfaces in cementitious materials. J Eng Mech 124(7):775–782

Kranz RL, Scholz CH (1977) Critical dilatant volume of rocks at the onset of tertiary creep. J Geophys Res 82(30):4893–4898

Leckie FA, Hayhurst DR (1974) Creep rupture of structures. Royal Society Math Phys Eng Sci 340(1622):323–347

Mazars J (1984) Application of damage mechanics to non linear behavior and failure of concrete in structures (in french). Phd thesis, University Paris, Paris, France

Munson D, Dawson P (1984) Salt constitutive modeling using mechanism maps. In: First International Conference on the Mechanical Behavior of Salt, Trans. Tech. Publications, Clausthal, Germany, pp 717–737

Nebozhyn MV, Gilormini P, Ponte Castañeda P (2001) Variational self-consistent estimates for cubic viscoplastic polycrystals: the effects of grain anisotropy and shape. Journal of the Mechanics and Physics of Solids 49(2):313–340

Nemat-Nasser S, Hori M (1993) Micromechanics: overall properties of heterogeneous solids. Appl Math Mech, Elsevier, Amsterdam

Pouya A (1991) Comportement rheologique du sel gemme application a l'etude des excavations souterraines. PhD thesis, Ecole Nationale des Ponts et Chaussées, Paris

Pouya A (2000) Micro-macro approach for the rock salt behaviour. Eur J Mech A/Solids 19:1015–1028

Pouya A (2015) A finite element method for modeling coupled flow and deformation in porous fractured media. Int J Numer Anal Methods Geomech (under review)

Pouya A, Zhu C, Arson C (2015) Micro-macro approach of salt viscous fatigue under cyclic loading. Mechanics of Materials (under review)

Senseny P, Hansen F, Russell J, Carter N, Handin J (1992) Mechanical behaviour of rock salt: phenomenology and micromechanisms. Int J Rock Mech Min Sci Mech Abstr 29(4):363–378

Skrotzki W, Haasen P (1984) The role of cross slip in the steady state creep of salt. In: second conference on the mechanical behavior of salt September, pp 24–28

Urai JL, Spiers CJ, Zwart HJ, Lister GS (1986) Weakening of rock salt by water during long-term creep. Nature 324:554–557

Wanten PH, Spiers CJ, Peach CJ (1996) Deformation of nacl single crystals at 0.27 tm. Series on Rock and Soil Mech 20:117–128

Warren J (2006) Evaporites:Sediments, Resources and Hydrocarbons. Springer

Weng G (1982) A unified self-consistent theory for the plastic-creep deformation of metals. J Appl Mech 49:728–734

Yang C, Daemen J, Yin J (1999) Experimental investigation of creep behavior of salt rock. Int J Rock Mech Min Sci 36(2):233–242

Zhu C, Arson C, Pouya A (2015) Theoretical and numerical matrix-inclusion models of damage accommodation in salt subject to viscous fatigue. In: Mechanical Behavior of Salt VIII, Rapid City, SD, USA